Red blood cells tracking and cell-free layer formation in a microchannel with hyperbolic contraction: A CFD model validation

Maria Gracka [a,*], Rui Lima [b,c], João M. Miranda [c], Sebastian Student [d,e], Bartłomiej Melka [a], Ziemowit Ostrowski [a]

[a] Department of Thermal Technology, Biomedical Engineering Laboratory, Silesian University of Technology, Gliwice, Poland
[b] MEtRiCS, DME, School of Engineering, University of Minho, Braga, Portugal
[c] CEFT, Faculdade de Engenharia da Universidade do Porto (FEUP), Porto, Portugal
[d] Department of Systems Biology and Engineering, Silesian University of Technology, Gliwice, Poland
[e] Biotechnology Centre, Silesian University of Technology, Gliwice, Poland

ARTICLE INFO

ABSTRACT

Background and Objective: In recent years, progress in microfabrication technologies has attracted the attention of researchers across disciplines. Microfluidic devices have the potential to be developed into powerful tools that can elucidate the biophysical behavior of blood flow in microvessels. Such devices can also be used to separate the suspended physiological fluid from whole in vitro blood, which includes cells. Therefore, it is essential to acquire a detailed description of the complex interaction between erythrocytes (red blood cells; RBCs) and plasma. RBCs tend to undergo axial migration caused by occurrence of the Fåhræus-Lindqvist effect. These dynamics result in a cell-free layer (CFL), or a low volume fraction of cells, near the vessel wall. The aim of the paper is to develop a numerical model capable of reproducing the behavior of multiphase flow in a microchannel obtained under laboratory conditions and to compare two multiphase modelling techniques Euler-Euler and Euler-Lagrange.
Methods: In this work, we employed a numerical Computational Fluid Dynamics (CFD) model of the blood flow within microchannels with two hyperbolic contraction shapes. The simulation was used to reproduce the blood flow behavior in a microchannel under laboratory conditions, where the CFL formation is visible downstream of the hyperbolic contraction. The multiphase numerical model was developed using Euler-Euler and hybrid Euler-Lagrange approaches. The hybrid CFD simulation of the RBC transport model was performed using a Discrete Phase Model. Blood was assumed to be a nonhomogeneous mixture of two components: dextran, whose properties are consistent with plasma, and RBCs, at a hematocrit of 5% (percent by volume of RBCs).
Results: The results show a 5 μm thick CFL in a microchannel with a broader contraction and a 35 μm thick CFL in a microchannel with a narrower contraction. The RBC volume fraction in the CFL is less than 2%, compared to 7–8% in the core flow. The results are consistent for both multiphase simulation techniques used. The simulation results were then validated against the experimentally-measured CFL in each of the studied microchannel geometries.
Conclusions: Reasonable agreement between experiments and simulations was achieved. A validated model such as the one tested in this study can expedite the microchannel design process by minimizing the need to prefabricate prototypes and test them under laboratory conditions.

1. Introduction

The rapid development of micromechanics during the last decades and the tendency to miniaturization led to an increase in the relevance of microfluidic systems in life sciences. The well-known benefit of microscale analysis is the ability to carry out separation and detection with high resolution and sensitivity and perform multiple measurements simultaneously with the same efficiency, in the smallest possible volume. Microfluidic devices, commonly termed Lab-on-a-Chip (LOC), are integrated onto one chip that may provide the same functions as those initially conducted inside laboratories. Such devices are often complex op-

* Corresponding author.
E-mail address: maria.gracka@polsl.pl (M. Gracka).

toelectronic laboratories built on a surface of the order of one square centimeter [1]. Analysis performed with LOC allows the minimised sample consumption, leading to reduced waste and costs and the ability to carry out more experiments [2]. Microfluidic technologies combine engineering, physics, chemistry, nanotechnology, biotechnology, and medical issues, hence can be used in various branches, from miniaturization of molecular biology reactions to cell growth and analysis platforms. Microfluidic devices use constructions based on passive (capillary) and active fluid flow through microscopic vessels [3]. Biologically, it seems particularly important, as most processes involve microflow from transport through cell walls, oxygen diffusion into the lungs, and blood flow in the capillaries [4]. LOCs has found applications in cell sorting, such as a label-free separation method to detect circulating tumour cells in blood [5] or blood cells isolated from plasma [6], can be used to measure whole blood flow velocity during coagulation [7], moreover it is possible to study in vitro environment the RBCs deformability in channels simulating capillaries [8]. Additionally, in biomedical engineering, LOCs can be used to create tissues [9] and organs on a chip that mimics the cardiovascular system's functions, mechanics, and physiological responses and can be applied as platforms for studying pathogens [10]. Detailed and high-throughput analysis of the biophysical behavior of the blood flow is crucial for a better understanding of the phenomena occurring in a human cardiovascular system which is designed to ensure the survival of all cells of the body. Blood has a particular role in the human body. It provides the transport of oxygen and nutrients to cells and the transport of metabolism products, ensures communication between individual body systems, and guarantees defence functions as a part of the immune system. Blood is a suspension of blood cells in a viscous plasma fluid. This nonhomogeneous mixture consists of plasma and suspended within erythrocytes, leukocytes, thrombocytes, and platelets [11]. Red blood cells are the primary type of blood cells with the hematocrit nearly half of the blood's volume (40%-45%). Human erythrocyte with biconcave shape and an average diameter of 8 μm has a usual life span of 120 days. RBCs are in charge of the supply of oxygen from the lungs to all body tissues. Additionally, they are specialized in the removal of carbon dioxide and metabolic wastes from tissues [12]. In microcirculation, blood flow behavior depends on several combined effects such as cell deformability, flow shear rate, and geometry of the microvessel. Hence, it is crucial to acquire a detailed description of the complex interaction between erythrocytes and plasma [13].

As blood flow occurs, RBCs tend to move to the center of the vessel they travel through. This physiological phenomenon is known as the Fåhræus-Lindqvist effect [14]. Studies have shown that the viscosity of blood changes with the diameter of the vessel, in particular, the apparent viscosity continues to decrease as the diameter decreases [12]. Consequently, this tendency leads to the formation of two regions, i.e., a cell-free layer close to the wall and a flow core with mainly RBCs. Understanding the CFL behavior in microcirculation is essential as it contributes to the rheological properties of the blood in microvessels. Performed experiments [15,16] demonstrated that depending on the geometry of the microfluidic device, using various shapes of the hyperbolic contraction of the microchannel, it is possible to obtain a different value of the CFL thickness. A microchannel composed of the hyperbolic contraction followed by an abrupt expansion allows the separation of the RBCs from plasma. The study of the contraction shape influence on the CFL thickness requires microchip fabrication and experimentation.

Therefore, the main objective of this work is to develop a numerical model capable of reproducing the multiphase flow behavior in a microchannel obtained under laboratory conditions. The development of such simulations can help select the optimal channel geometry while ensuring shorter prototyping and testing time

and reducing microchip production costs. In the last few decades, Computational Fluid Dynamics has become a powerful tool for flow modelling and proved its applicability in biomedical blood flow simulation [17]. Some mathematical models can be used for modelling multiphase blood flow, like Euler-Euler [18] or hybrid Euler-Lagrange techniques [19]. The multiphase approach in blood modelling allows one to preserve all information regarding the properties and distribution of the blood components. Often in numerical simulations, the plasma is modelled to behave as a Newtonian fluid while suspended within rigid spherical particles that have viscosity dependent on the shear rate and hematocrit [11]. In the available literature, studies can be found showing the experiments for testing the RBCs deformability. In the conducted experiments, to investigate the motion of the particles, the authors use different sizes of microchannels contractions corresponding to the structure of capillaries [20]. Based on the conditions of the experiment, numerical models were built using the Finite Element Method to simulate the behavior and deformation of "healthy" and "sick" RBCs [21]. In [22] simulation was developed to separate erythrocytes according to their mechanical properties, changing with pathological conditions such as malaria infection. The RBCs flow behavior, including shape change due to high shear rates, can be simulated using fluid-structure coupling. The implementation is performed by the immersed boundary method adapted to unstructured grids. The simulation method relies on the finite-volume parallel solver for incompressible Navier-Stokes equations on unstructured meshes. The discretization of RBCs is performed by a moving Lagrangian mesh and modelled as viscous drops enclosed by membranes resisting shear, bending, and area dilation [23]. The current publication compares applications of the Euler-Euler and Euler-Lagrange approaches in the modelling of the two-phase blood flow in a hyperbolic contraction of the microchannel.

The proposed CFD model simulates the process of CFL formation in microchannels with hyperbolic contraction. The numerical model was developed to reproduce the RBC movement visualised and recorded under laboratory conditions [16]. The multifluid Euler-Euler (E-E) and hybrid Euler-Lagrange (E-L) approaches were used to model the following: continuous phase (Dx40) and suspended particles (RBCs). To the best knowledge of the authors, this is the first research where those two models were applied and compared against experimental results in the microchannel application. The main simplification in the E-L model is the round shape of the particles. However, this simplification was estimated to be acceptable on the basis of research [24]. The performed validated simulations showed that the hybrid E-L model allows to better represent the red blood cell flow behavior than model based on E-E approach. A better prediction of the flow by E-L model occurred mainly in the cell-free layer region of the investigated microchannels. Therefore, the authors recommend to choose the E-L approach for similar problems.

2. Methods

2.1. Geometrical model

The geometries of two hyperbolic-shaped microchannels, previously described and studied in [16], were used to develop a numerical model to simulate and investigate the formation of the CFL. The contraction shapes were chosen according to the Hencky strain (e_H) value defined by Eq. (1).

$$e_H = ln\left(\frac{h}{w}\right) \tag{1}$$

where h and w are the channel and contraction widths, respectively. The microchannel geometry signed A consists of one hyperbolic contraction with a throat width of 54 μm and Hencky strain
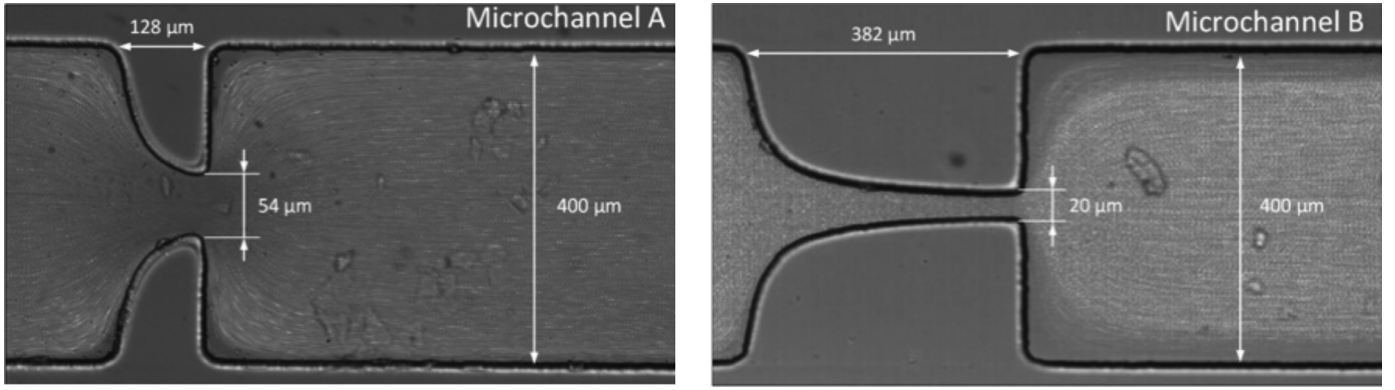
Fig. 1. Main dimensions of microchannel type A and type B.

$e_H = 2$. The microchannel labelled as B consists of a wider narrowing of 20 µm and Hencky strain $e_H = 3$. The height of both microchannels is 50 µm. Channel A and B consist of input and output ports to which syringes are connected to deliver and drain the mixture, the main part of the channel is 400 µm wide and there is a narrowing on this part in both channels. The ports are at a significant distance from the constriction and therefore could be omitted from the simulation. The length of the channel including the ports is 12 mm, the length of the main channel from port to the narrowing is 2.3 mm. Dimensions of the microchannels in the area of hyperbolic contraction are shown in Fig. 1.

2.2. Numerical mesh

The presented geometry was used for numerical discretization, and four different size numerical meshes were tested for each microchannel. The discretization selection criterion was based on the particle volume fraction distribution in the channel area downstream of the hyperbolic contraction. The tested meshes were selected due to a discretization sensitivity study based on the element number increment procedure in the domain.

For the geometry of microchannel A, meshes consisting of over 600 k, 800 k, 900 k, and 1 M elements were tested. The analysis showed that a further increase in the number of elements did not affect the obtained results. Therefore, the generated hybrid mesh consists of over 915 k elements. In the location of hyperbolic contraction, the mesh is unstructured and consists of tetrahedral elements. In the inlet and outlet ports and channel, the structural mesh was generated with hexahedral elements.

For the final mesh used in these simulations, the orthogonal quality range was 0.44 to 1, where over 80% of elements have an orthogonal quality value higher than 0.85. The cell skewness range was 0 to 0.64, where over 90% of elements have a skewness value lower than 0.35.

For the geometry of microchannel B, meshes consisting of 700 k, 900 k, 1 M, and 1.2 M elements were tested. Finally, in the simulation, a mesh consisting of 1 M elements was used. Increasing the number of cells to 1.2 M did not affect the obtained results. Similarly to microchannel A, the numerical mesh in the contraction area is unstructured and consists of tetrahedral elements while, in the rest of the domain, a hexahedral structural mesh was formed. For the final mesh, the cell orthogonal quality range was 0.35 to 1, where over 90% of elements have an orthogonal quality value higher than 0.68. The cell skewness ranges from 0 to 0.73, where over 90% of elements have a skewness value lower than 0.48. The overview of the numerical mesh used to simulate the flow in microchannels A and B are shown in Fig. 2.

Tab. 1 shows the value of the maximum and mean relative error of the calculated RBCs velocity depending on the mesh size.

The sensitivity analysis shows that the flow simulation using the E-L model is not strongly dependent on the number of elements, it is more significant when using the E-E model, so the mesh selection was based on the determined values for this approach. Further increasing the mesh size did not influence the error reduction. The meshes selected allowed to limit in computational cost giving satisfactory results.

2.3. Multiphase model

The first technique used to model multiphase flow was the Euler-Euler approach [17], while both phases are treated as interpenetrating continua with defined physical properties. The E-E approach uses a set of transport equations, including the mass and momentum conservation equation, to describe particle transport in the microchannel. The continuity transport equations for dextran (fluid phase) and RBCs (solid phase) are shown in Eq. (2) and Eq. (3), respectively. In contrast, Eq. (4) and Eq. (5) define the equations for the conservation of momentum for the fluid and solid phases, respectively [25]:

$$\frac{\partial(\varepsilon_f \rho_f)}{\partial t} + \nabla \cdot (\varepsilon_f \rho_f \mathbf{u}_f) = 0 \tag{2}$$

$$\frac{\partial(\varepsilon_s \rho_s)}{\partial t} + \nabla \cdot (\varepsilon_s \rho_s \mathbf{u}_s) = 0 \tag{3}$$

$$\frac{\partial(\varepsilon_f \rho_f \mathbf{u}_f)}{\partial t} + \nabla \cdot (\varepsilon_f \rho_f \mathbf{u}_f \mathbf{u}_f) = -\varepsilon_f \nabla p + \nabla \cdot \tau_f + \varepsilon_f \rho_f \mathbf{g} + \beta(\mathbf{u}_s - \mathbf{u}_f) \tag{4}$$

$$\frac{\partial(\varepsilon_s \rho_s \mathbf{u}_s)}{\partial t} + \nabla \cdot (\varepsilon_s \rho_s \mathbf{u}_s \mathbf{u}_s) = -\varepsilon_s \nabla p + \nabla \cdot \tau_s + \varepsilon_s \rho_s \mathbf{g} + \beta(\mathbf{u}_f - \mathbf{u}_s) \tag{5}$$

where subscripts f and s correspond to the fluid and solid phases respectively, ϵ is the phase volume fraction, $\mathbf{g}$ is the gravity vector, ρ is the density, $\mathbf{u}$ defines the velocity vector, p is the pressure of the fluid phase, and β represents the interphase exchange coefficients between phases. The interphase exchange coefficient between fluid and solid phases depends on the particle volume fraction. The model of Wen and Yu [26] appropriate for dilute systems (the volume fraction of the fluid is greater than 0.8) and given by Eq. (6) was used in the simulation.

$$\beta = \frac{3}{4} C_D \frac{\varepsilon_s \varepsilon_f \rho_f |\mathbf{u}_s - \mathbf{u}_f|}{d_s} \varepsilon_f^{-2.65} \tag{6}$$

where d_s is a particle diameter, C_D presented in Eq. (7) represents the drag coefficient.

$$C_D = \frac{24}{\varepsilon_f \mathrm{Re}_s}[1 + 0.15(\varepsilon_f \mathrm{Re}_s)^{0.687}] \tag{7}$$
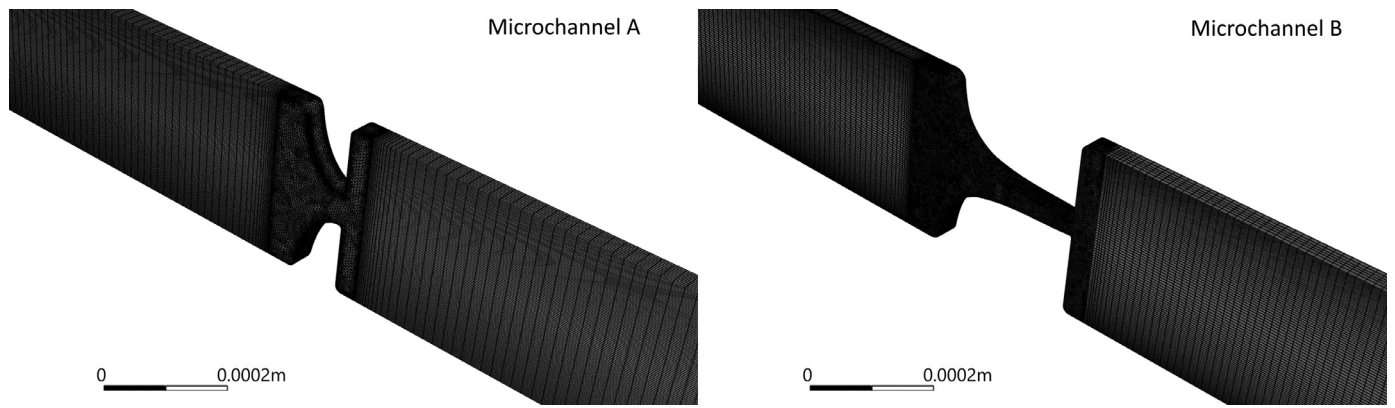
Fig. 2. Numerical mesh in hyperbolic contraction region of microchannel type A and type B.

Table 1
Mesh sensitivity summary.

	Microchannel A				Microchannel B			
	Euler-Euler model							
Mesh size	600k	800k	915k	1M	700k	900k	1M	1.2M
Velocity mean rel. error (core flow only)	10.3%	9.7%	8.0%	7.9%	8.5%	6.9%	6.3%	6.3%
Velocity max. rel. error (core flow only)	15.4%	14.9%	14.3%	14.2%	12.9%	12.4%	11.9%	11.9%
Velocity mean rel. error	18.0%	17.5%	17.1%	17.1%	17.0%	16.5%	15.8%	15.8%
Velocity max. rel. error	87.4%	86.5%	85.3%	85.3%	84.0%	82.2%	81.9%	81.9%
CFL thickness	8 μm	7 μm	5 μm	5 μm	40 μm	40 μm	35 μm	35 μm
	Euler-Lagrange model							
Velocity mean rel. error	3.5%	3.1%	2.9%	2.9%	2.5%	2.1%	1.9%	1.9%
Velocity max. rel. error	6.8%	6.0%	5.6%	5.6%	4.1%	3.8%	3.4%	3.4%
CFL thickness	8 μm	8 μm	5 μm	5 μm	40 μm	35 μm	35 μm	35 μm

where Re_s shown in Eq. (8) defines the relative Reynolds number.

$$Re_s = \frac{\rho_f d_s |\mathbf{u}_s - \mathbf{u}_f|}{\mu_f} \tag{8}$$

The τ_f presented in Eq. (9) and τ_s in Eq. (10) are the fluid and solid stress tensors, respectively, representing the viscous forces in the fluid phase [17].

$$\tau_f = \varepsilon_f \mu_f (\nabla \mathbf{u}_f + \nabla \mathbf{u}_f^T) - \frac{2}{3} \varepsilon_f \mu_f \nabla \cdot \mathbf{u}_f \bar{\mathbf{I}} \tag{9}$$

$$\tau_s = \mu_s (\nabla \mathbf{u}_s + \nabla \mathbf{u}_s^T) + (\zeta_s - \frac{2}{3}\mu_s) \nabla \cdot \mathbf{u}_s \bar{\mathbf{I}} \tag{10}$$

where μ_f represents the dynamic fluid viscosity, μ_s is shear viscosity defined, ζ_s is the bulk viscosity expressed as a function of granular temperature θ given by Eq. (14) and $\bar{\mathbf{I}}$ is the unit tensor. Dextran is considered a Newtonian fluid with constant viscosity (μ_s), and the non-Newtonian properties of the mixture are due to the RBC viscosity model since the rheological properties of human blood depend not only upon shear rate but also upon hematocrit [27]. In the Euler-Euler approach, RBC viscosity was calculated using the modified Carreau-Yasuda viscosity model in Eq. (11).

$$\eta = \frac{\varepsilon_s \mu_s + \varepsilon_f \mu_f}{\mu_f} = m \left[1 + (\lambda \dot{\gamma})^2 \right]^{(n-1)/2} \tag{11}$$

where η is the relative mixture viscosity, ε_s and ε_f are volume fractions of RBCs and plasma, respectively, μ_s and μ_f are RBCs and plasma viscosity, respectively, n and m are parameters, and $\dot{\gamma}$ is the shear rate. The time constant λ is taken as 0.110 s, and the plasma viscosity is assumed as a Newtonian fluid with constant value. Eq. (12) and Eq. (13) show the correlation for constants n and m as a function of hematocrit H, which in this model is equal to RBC volume fraction [27].

$$m = 122.28H^3 - 51.213H^2 - 16.305H + 1 \tag{12}$$

and

$$n = 0.8092H^3 - 0.8246H^2 - 0.3503H + 1 \tag{13}$$

The Carreau-Yasuda viscosity model was implemented in the commercial ANSYS Fluent code using the so-called User Defined Function (UDF).The bulk viscosity is expressed by Eq. (14).

$$\zeta_s = \frac{4}{3} \varepsilon_s^2 \rho_s d_s g_0 (1+e) \left(\frac{\theta}{\pi} \right)^{1/2} \tag{14}$$

where e is the restitution coefficient and g_0 is the radial distribution function defined in Eq. (15).

$$g_0 = \left[1 - \left(\frac{\varepsilon_s}{\varepsilon_{s,max}} \right)^{1/3} \right]^{-1} \tag{15}$$

The sum of the volume fraction for each phase sums to one expressed by Eq. 16.

$$\varepsilon_f + \varepsilon_s = 1 \tag{16}$$

The second applied technique of the multiphase flow modelling, in contrary to Euler-Euler, was the hybrid Euler-Lagrange multiphase approach [28]. In this approach, the fluid phase is treated as a continuum by solving the Navier-Stokes equations, while the dispersed phase is solved by tracking a large number of particles through the calculated flow field. A Discrete Phase Model (DPM) is used in the Lagrangian frame of reference to track particle motion, whereas an Eulerian formulation is simultaneously used for the continuous phase. The DPM is valid for solid phase volume fractions less than 10% [29]. Therefore, this hybrid technique can be used for RBCs flow simulation in the current research, due to the experimental conditions where the particle volume fraction is 5%. When the dispersed phase occupies a low volume fraction, the particle-particle interaction can be neglected, making the approach considerably simpler. The one-way coupling scheme is ap-

plied when the particle volume fraction is lower then 10%. For one-way coupling calculations in ANSYS Fluent, only the fluid pressure acting on the structure is transferred to the structure solver [30].

The DPM approach does not solve the momentum equation for an individual particle. Instead, the solver tracks groups of particles called parcels. Each parcel contains several particles characterised by the same mass, velocity, and position. In this model, each parcel is tracked separately within the continuous phase. The number of individual particles contained in a parcel for injection boundary condition can be calculated form Eq. (17)

$$n_p = \frac{\dot{m}_{parcel} \Delta t}{m_p} \qquad (17)$$

where Δt is the time step in transient calculation, $\dot{m}_{parcel}$ is the mass flow rate of a parcel and m_p is the mass of an individual particle estimated from the particle diameter and density. The DPM requires calculating the force balance equation for each parcel as shown in Eq. (18); this allows us to predict the trajectory of a discrete phase particle. This force balance equates the particle inertia with the forces acting on the particle [31]

$$\frac{d\mathbf{u}_p}{dt} = F_D(\mathbf{u}\text{-}\mathbf{u}_p) + \frac{\mathbf{g}(\rho_p - \rho)}{\rho_p} - \frac{\nabla p}{\rho_p} - \frac{\nabla \cdot \sigma_p}{\rho_p} \qquad (18)$$

where the term $F_D(\mathbf{u}\text{-}\mathbf{u}_p)$ defines the particle acceleration due to the drag in Eq. (19), the term $\frac{-\nabla p}{\rho_p}$ defines the particle acceleration due to the pressure difference at the particle location and σ_p is granular stress tensor [32].

$$F_D = \frac{3\mu C_D \text{Re}_p}{4\rho_p d_s^2} \qquad (19)$$

where Re_p is the relative Reynolds number defined as Eq. (8), d_p is particle diameter and C_D is the drag coefficient defined as

$$C_D = a_1 + \frac{a_2}{\text{Re}_p} + \frac{a_3}{\text{Re}_p} \qquad (20)$$

where a_1, a_2, a_3 are constants, describing the drag coefficient function depending on the Reynolds number value [33].

The basic mass balance equation for the fluid is calculated using the Eulerian approach from Eq. (2) and for the dispersed phase with low volume fraction, it is calculated using a Lagrangian frame of reference as

$$\frac{\partial (\rho_s)}{\partial t} + \nabla \cdot (\rho_s \mathbf{u}_s) = S_i \qquad (21)$$

where S_i are the source terms for discrete phase momentum, energy, and species. Based on the calculated particle velocity, a new particle position can be expressed as

$$\frac{d\vec{x}_p}{dt} = \vec{v}_p \qquad (22)$$

After obtaining the particle position from Eq. (22), the volume fraction of the solid in a given cell can be calculated as

$$\varepsilon_p = \frac{n_p N_{parcel} V_p}{V_{cell}} \qquad (23)$$

where N_p is the number of particles in a parcel, N_{parcel} is the number of parcels in a cell, V_p is the volume of a particle, and V_{cell} is the volume of a cell. The calculated volume fraction is assigned to Eulerian coordinates, where the void fraction of the fluid can be determined as

$$\varepsilon_f = 1 - \varepsilon_s. \qquad (24)$$

Table 2
Properties of mixture components.

Dx40 density	1042	kg/m^3
Dx40 viscosity	0.0052	kg/(m·s)
RBCs density	1185	kg/m^3
RBCs diameter	8	μm

2.4. Simulation conditions

The numerical simulation conditions were set to reflect the nature of the performed experiments. The fluid used in the simulation was intended to fully mimic blood and assumes that blood is a nonhomogeneous mixture of two components: dextran 40 (Dx40), whose properties are consistent with plasma, and RBCs, at a hematocrit of 5% (percent by volume of RBCs). Tab. 2 gives the properties of dextran and RBCs [34]. The multifluid modelling techniques used in the simulation assumed the particles to be rigid spheres with a constant diameter of 8μm [17]. Studies show that adopting the simplification of modelling blood cells as rigid spheres can effectively mimic the dynamics of red blood cell flow in microchannels [24].

In actual flow, RBCs are deformable and this phenomenon is particularly evident in vessels with small diameters (close to the diameter of RBCs) and in diseased cases [35,36]. Blood flow in capillaries [37] where vascular branching occurs also affects changes in the shape of the erythrocytes [38]. In the literature, publications can present numerical models of particle deformation that present simulations of single-particle behavior [39,40]. Although particle deformation models are available, they are computationally expensive, especially in flows where a large number of particles are present. Research also uses models that introduce simplifications in the form of non-deformable particles. For vessels with diameters larger than the size of red blood cells, the assumption of rigid particles does not significantly affect the flow behavior of the blood mixture [24]. Simulation of rigid erythrocytes has as well been used to model two-phase blood flow in a vessel after a stent procedure [41]. Studies of rigidized red blood cells are also available in the literature to focus on the effects of rotational motions [42]. Simulations of the flow of the mixture that contains RBCs assumed to be rigid particles in channels of the order of 40 μm in diameter with bifurcation and contraction have also been performed [43]. Moreover, presented in the current research comparison of the E-E and E-L approaches was based on the same assumption that RBCs are rigid spherical solids. Despite this, the E-L technique showed a better prediction of the RBC behavior in the investigated microchannel.

The inlet boundary condition (BC) was set at a constant velocity of 0.0025 m/s, calculated from the volumetric flow measured during the experiment. The volumetric flow of the mixture was set to 10 μL/min. The outlet BC was considered a continuous outflow. The wall BC for plasma and RBCs was set to a no-slip velocity condition [44]. The flow was simulated as laminar due to low values of Reynolds number (Re < 0.1). The DPM was used to simulate the particle tracking in the hybrid Euler-Lagrange approach. The model uses the one-way coupling scheme due to the low concentration of RBCs. The additional inlet BC was set in the Euler-Lagrange model for particle injection. Constant particle mass flow of 1.406·10^{-8} kg/s was calculated using the Euler-Euler model. The parcel release method was set to a standard, and the number of injected particle parcels depended on the inlet surface mesh size.

3. Results

The simulated blood flow results for the Euler-Euler and hybrid Euler-Lagrange approaches are shown as color maps of the parti-
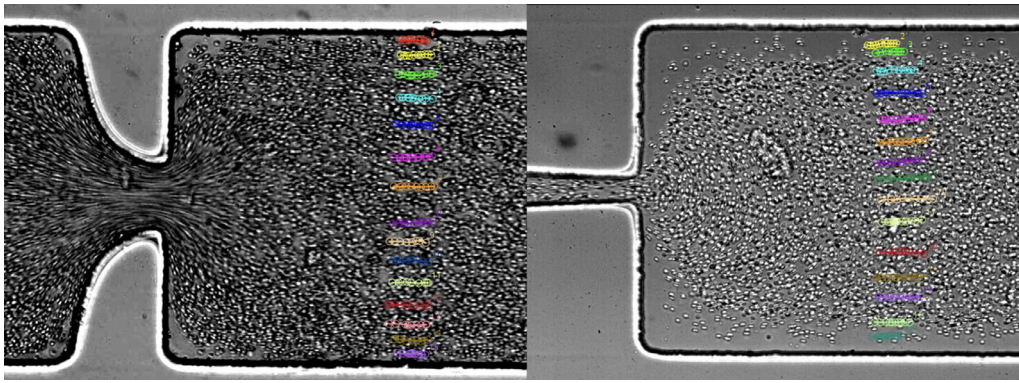
Fig. 3. Tracked RBCs paths in microchannel A (left) and B (right).

cle velocity field and the RBC distribution in the region of channel contraction. The numerical model results were validated using the in vitro experiment described by Rodrigues [16]. In the mentioned research, one can find a detailed description of the experimental part of the presented results used for validation procedure. In the published study, microchannels with several different numbers and contraction shapes were tested; however, two types were subject to numerical simulation in the study. The experiment was recorded with a high-speed imaging system consisting of an inverted microscope and a high-speed camera. A syringe pump was used to ensure a constant flow of 10 μl/min. A high-speed video microscopy system was used to control, visualise, and measure the working fluid that flows through hyperbolic microchannels and to record the video at a frequency of 3000 frames/s [16].

3.1. RBCs velocity validation

Velocities resulting from the numerical simulation were validated using the video recorded during the experiment. The open-source image analysis software ImageJ [45] was used for experimental data examination. A manual tracking plugin MTrackJ was used to track RBC particles individually. The manual method mimicked the classical particle image velocimetry (PIV) method. The velocity of the chosen RBCs was calculated by determining the position of the selected particles in several consecutive frames of the recorded movie. The calculation is based on the distances that a particle has traveled in a given time (the frequency of photo acquisition is also recorded). By calculating the particle flow velocity at different channel locations across the microchannel cross-section plane, it was possible to determine the RBC velocity profile downstream of the contraction. Fig. 3 shows the path of selected RBC particles and their positions in 10 consecutive video frames downstream of the contraction of the A (left) and B (right) microchannels, respectively. The selection of the experimental analysis method was made based on available literature sources presenting similar cases [44]. The selected positions of the cross-sections allow to estimate the RBCs velocity. In the region of the microchannel contraction, the velocity was too high to reliably estimate its value. It was caused by the limited speed and quality of the camera recordings.

The experimental image analysis shown in Fig. 4 is intended to visualize the particle concentration using the RBC max-intensity greyscale. The CFL thickness determined from the experiment was marked in the picture with a red dotted line. In Fig. 4, cross-sections A-A (left) and B-B (right) were marked to demonstrate the localisation of RBCs concentration obtained in the numerical simulation. A comparison of RBCs velocity results obtained from experimental analysis and CFD simulation is also presented for designated cross sections.

Fig. 5 shows the RBC velocity profile in the microchannel A calculated by CFD simulation and compared with experimental data. The velocity profile was generated at a distance of approximately 300 μm (cross-section A-A in Fig. 4) from the narrowing end.

Fig. 6 shows the RBC velocity profile in microchannel B obtained from the CFD simulation and compared with experimental data. The velocity profile was determined at a distance of approximately 300 μm (cross-section B-B in 4) from the end of the contraction.

3.2. RBC simulated velocity field

In the simulation of blood flow within the microchannel, the most critical indicator is the correctly-calculated velocity field within the channel. The velocity value and its profile affect the distribution of particles in the channel and the volume fraction profile. Therefore, the particle velocity in line with the experimental measurements can ensure the accuracy of determining flow characteristics, such as CFL thickness. First, the results of the velocity values and profile obtained in the numerical simulation were validated with the experiment [16].

The velocity field in microchannel A obtained with the E-E model is shown in Fig. 7 (a). Specifically, we show the particle velocity contour in a plane located along the flow at half the height of the channel and four cross-sections perpendicular to the flow. The highest velocity value of 0.2 m/s occurs in the area of narrowing. The particle velocities are evenly distributed in the channel core, where the particle velocity reaches 0.02 m/s, whereas near-wall velocity values are close to 0 m/s.

Fig. 7 (b) shows the RBC parcel position in the region of contraction calculated with the hybrid E-L technique and colored by the velocity magnitude. The obtained results are consistent with those achieved using the E-E technique. Again, the highest RBC velocity values of 0.2 m/s appear in the narrowing region, and the slowest particle flow occurs near the microchannel wall. In the channel core, RBC flow with a velocity of approximately 0.02 m/s. The E-L model allows for the computation of the velocity at a distance close to the channel wall (10 μm) in a more precise way compared to the E-E model. There are 5 rows of numerical grid cells in the boundary layer at a width of 10 μm from the vessel wall. The maximum velocity relative error in this region for DPM calculation reaches 5% compared to above 80% for the E-E approach and it occurs in the second layer of mesh cells.

The velocity contour plot in microchannel B obtained with the E-E approach is shown in Fig. 7(c). The highest RBC velocity value occurs in the region of contraction and reaches over 0.05 m/s. Near the wall, particle velocity is 0 m/s, and in the channel core, it is approximately 0.02-0.03 m/s. With four perpendicular cross-sections,
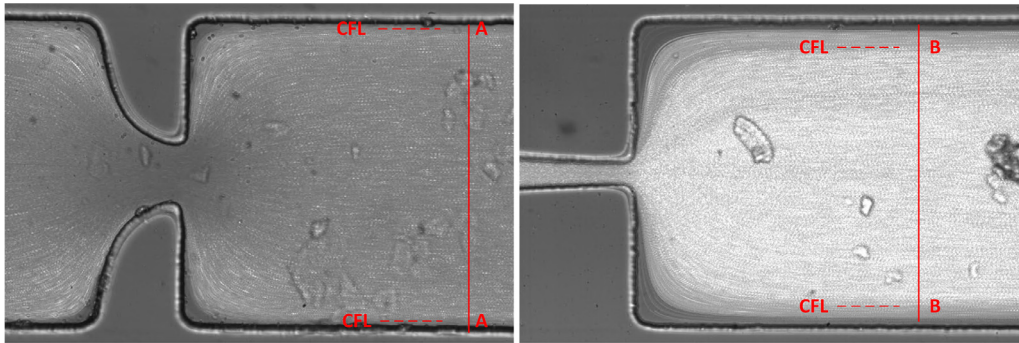
Fig. 4. Experimental CFL thickness in microchannel type A (left) and type B (right). Z project blood flow visualization using RBCs max-intensity gray scale in microchannel A and microchannel B.
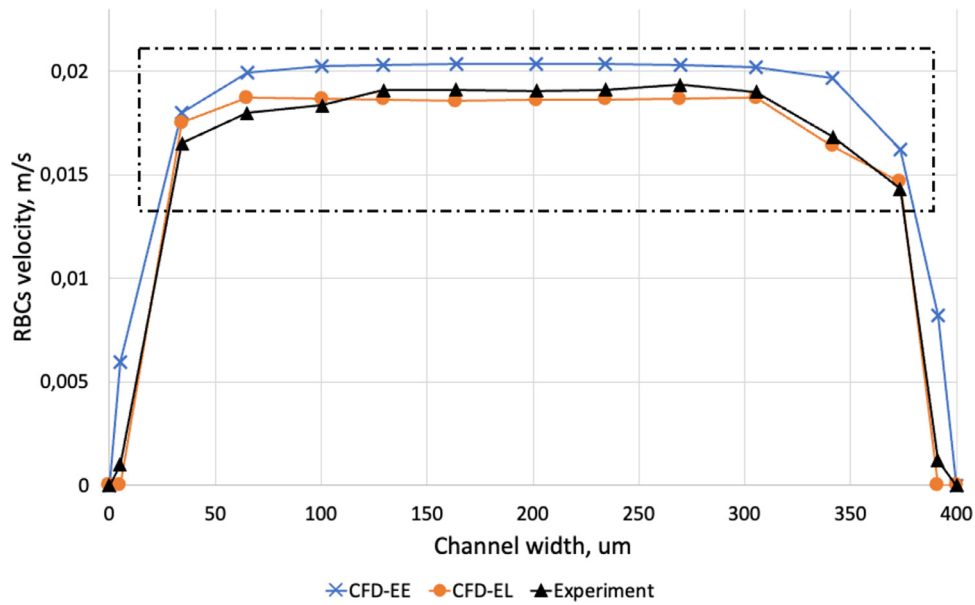

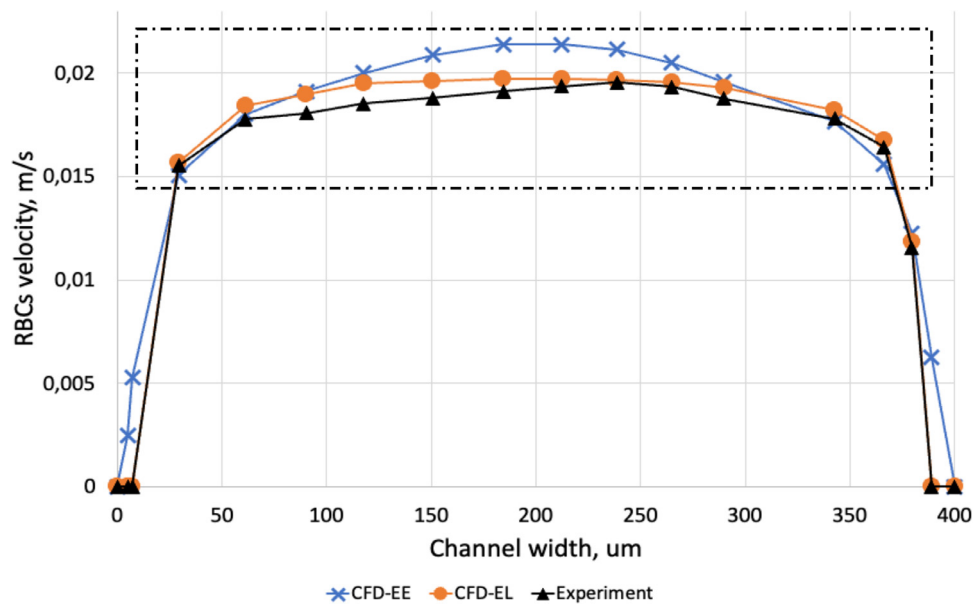**Fig. 5.** Microchannel A. Comparison of RBC velocity profile, CFD vs. experiment.

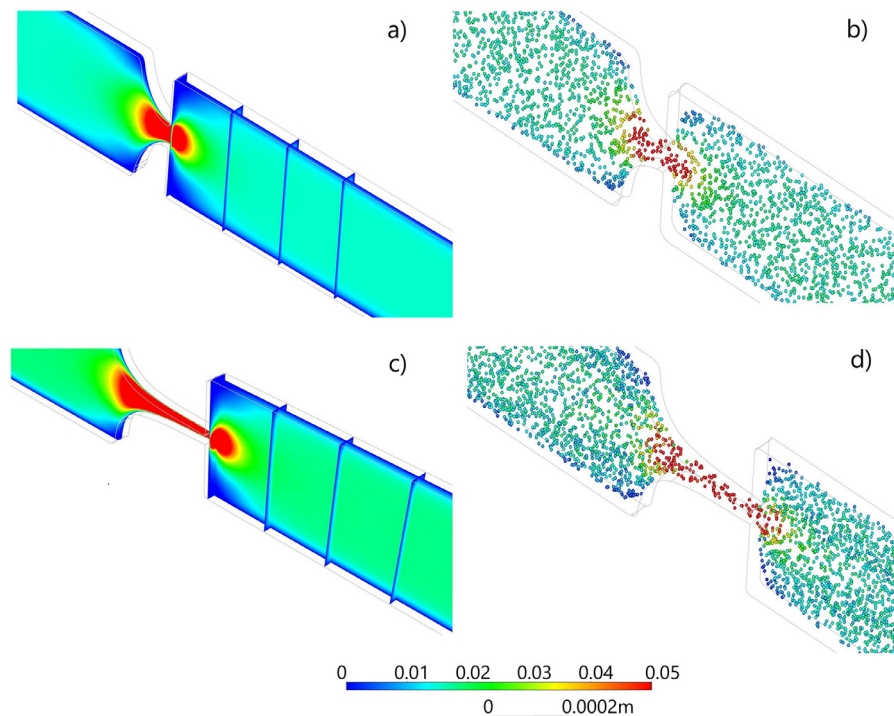**Fig. 6.** Microchannel B. Comparison of RBC velocity profile, CFD vs. experiment.

Fig. 7. Computed RBC velocity in microchannel a) type A using E-E, b) type A E-L and c) type B using E-E, d) type B E-L approach. CFD simulated particle velocity field shown as colormap and particle velocity shown as parcel position colored by velocity values (colormap velocity scale adjusted to show the particle velocity in the channel downstream of the constriction; red color corresponds to values above 0.05 m/s). (For interpretation of the references to colour in this figure legend, the reader is referred to the web version of this article.)

the zero particle velocity occurs near the top and bottom walls of the channel.

The DPM calculated velocity values are nearly identical (the average difference is less than 0.0012 m/s) compared to those obtained with the Euler-Euler technique. The highest value of 0.3 m/s occurs in the hyperbolic contraction, and the lowest is near the wall of the channel. Particle velocity in the core reaches approximately 0.02-0.03 m/s. Fig. 7 d) shows each particle's parcel position colored by the velocity value.

3.3. CFL thickness validation

Due to the large number of RBCs, the open-source ImageJ software [45] used in experimental analysis does not quantify the volume fraction of the cell suspension in the mixture since the recording shows particles in the entire channel volume. The experimental data analysis enables us to define the qualitative profile of RBC volume fraction in the core of the microchannel. The Z project built-in ImageJ software plugin uses greyscale intensity to determine the concentration of particles in the cross-section parallel to the flow direction. Based on the generated profile, it is possible to estimate the CFL thickness.

In Fig. 8, the numerical simulations for RBCs distribution in microchannel A are shown. The graph on the left side shows the particle volume fraction in the cross-section A-A obtained with the E-E approach. The CFL thickness determined in the experimental analysis is marked with red lines on both channel sides. The computed results show a sudden increase in the RBC volume fraction within approximately 5 μm from the channel wall, matching experimental value. The graph on the right side shows the RBC concentration obtained with the E-L approach. The concentration of the particles is close to 0 kg/m³ at a 5 μm distance from the wall and starts to increase beyond this distance. In the channel core, cell concentration reaches on average 70 kg/m³. The compar-

ison of the obtained numerical results and the experiment analysis in microchannel B is shown in Fig. 9. The volume fraction profile calculated with the E-E approach is shown on the left side of Fig. 9 and compared with the experimental value plotted (red lines). The simulated CFL thickness reaches 35 μm from the channel wall where the volume fraction exceeded 2%. The E-E model shows the smooth formation of the CFL compared to the relatively sharp formation simulated with the E-L approach. The RBC concentration profile calculated with the E-L model presented on the right side of Fig. 9 shows that the sudden increase in particle numbers occurs at a 35 μm distance from the channel B wall. In the CFL, RBC concentration is less than 10 kg/m³ while, in the channel core, the average concentration is 60 kg/m³. The simulation results match the experimental data.

3.4. Simulated RBC volume fraction distribution

The volume fraction distribution of the RBCs obtained with the E-E model is shown in Fig. 10 a).

The RBC distribution obtained in the numerical simulation was visually compared with the experimental data. The greyscale experimental image is visible in the background, while the simulated RBC distribution is shown as an overlaid colormap. The blue color on the contour plot corresponds to a particle volume fraction lower than 2%. The CFL thickness obtained with the E-E approach equals approximately 5 μm and is consistent with the experimental results. The simulated volume fraction of the RBCs in CFL is less than 2% compared to 6% in the core flow. The DPM model used in the hybrid E-L technique allows us to determine the particle concentration in the computational domain. The calculated RBC concentration in the contraction region is shown in Fig. 10 (b) as parcels colored by RBC concentration value. The grayscale experimental image is visible in the background. Simulated flow in the microchannel B hyperbolic contraction is shown in Fig. 10 (c) as
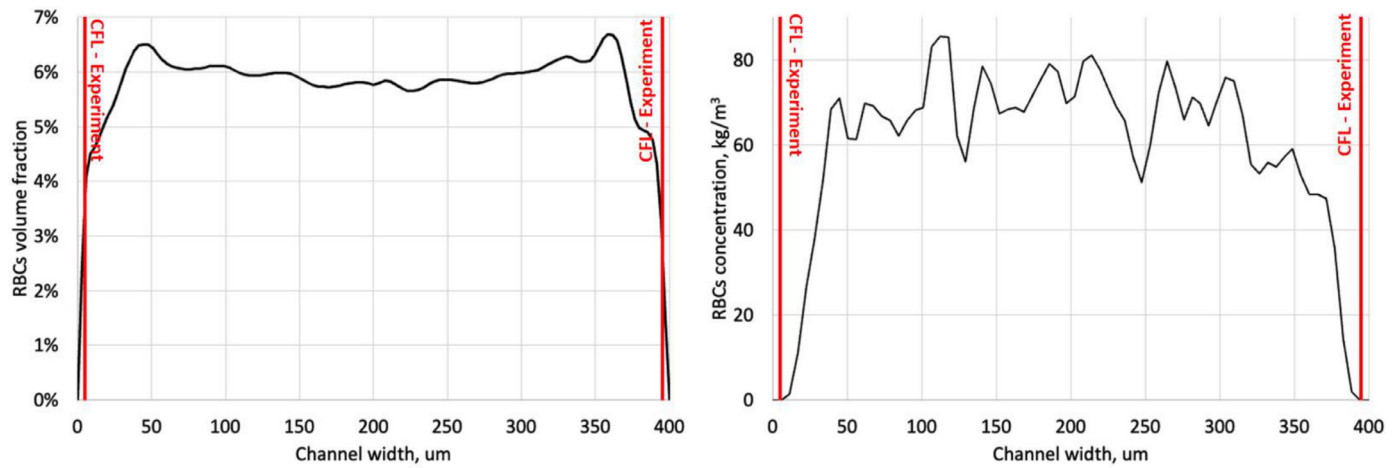
Fig. 8. Computed RBC distribution in microchannel type A using E-E (left) and E-L (right). The RBC volume fraction distribution in the cross-section A-A for E-E technique (left) and the RBC concentration profile for the E-L technique (right).
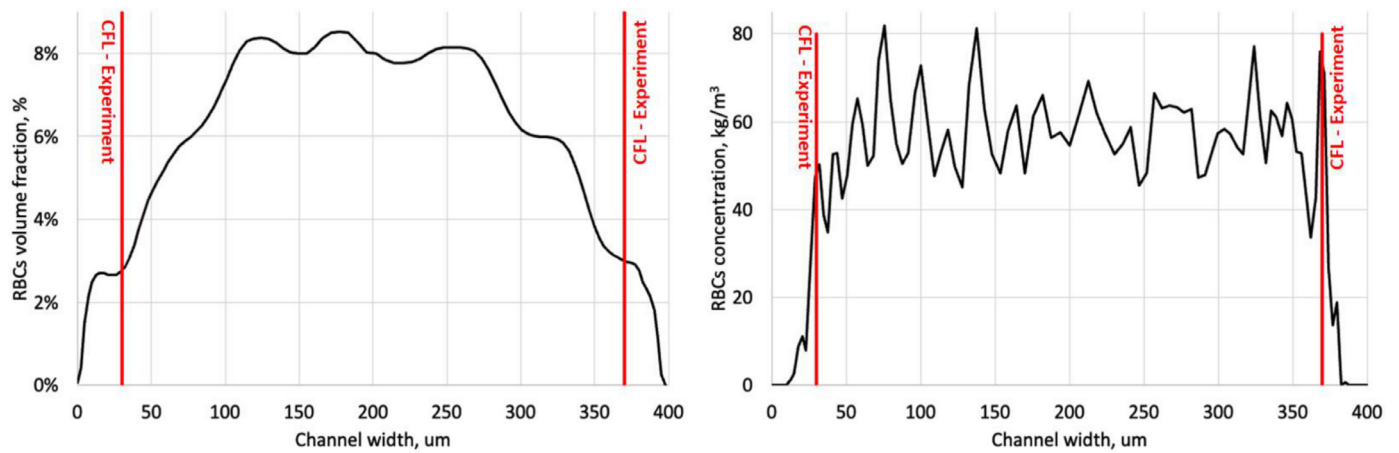

Fig. 9. Computed RBC distribution in microchannel type B using E-E (left) and E-L (right). The RBC volume fraction distribution in the cross-section B-B for the E-E technique (left) and the RBC concentration profile for the E-L technique (right).

a colormap of RBC volume fraction distribution obtained with the E-E approach. The solution was compared with the experimental data shown as an image in the background. Red dotted lines represent the CFL thickness determined from experimental analysis. The CFL thickness in the CFD model was defined at the location where RBC volume fraction exceeds 2%. The simulated CLF thickness reached 35 μm. Fig. 10 (d) shows the position of the particle in the area of contraction obtained with the E-L approach and compared with the experimental image in the background. In the CFL, the particle concentration was 0 to 10 kg/m^3.

4. Discussion

In the following section results presented in Section 3 are discussed. The numerical model adequately predicted the nature of the RBC flow in microchannels with hyperbolic contraction. The obtained velocity profile and RBC distribution characteristics are in good agreement with the experimental data analysis [16].

Microchannel type A: The velocity values calculated with E-E approach are marginally higher than the experimental values (Fig. 5). Specifically within the channel core, the velocity values are on average 0.0018 m/s higher than in the experiment. The highest discrepancy occurs in the area of the boundary layer at a 10 μm distance from the wall, where the maximum velocity difference is 0.0051 m/s. The better representation of the RBCs flow behavior by

E-L approach can be caused by Langrangian concept of the particle tracking, which can predict different parcel position in single cell. This concept of parcel tracking in some way reduces the influence of the mesh resolution into the prediction of the RBC particle modelling. In contrary, E-E approach allows only to estimate one velocity for each specified cell for all simulated RBC particles within this cell on the base of volume fraction. Therefore, in the E-E approach, the mesh resolution strongly affects the prediction of RBC in zones such as cell-free layer. The hybrid E-L approach gives more accurate values with slightly higher discrepancies in the boundary layer. The highest velocity difference for the E-L model occurs in the channel core and reaches 0.0012 m/s only, while the average difference in the core is 0.0005 μm.

Microchannel type B: Fig. 6 shows that the numerical simulation results are in good agreement with the analysis of experimental measures. Better consistency of flowing RBC velocity was obtained using the hybrid E-L model, and it is especially noticeable near the boundary layer. The average computed velocity difference compared to experimental values is 0.0004 m/s. The differences occur in the channel core, and the highest velocity discrepancy reached 0.0012 m/s. The E-E model gives marginally overstated velocity values in the channel core, where the average difference is 0.0011 m/s. The largest discrepancies in the calculated values of RBC velocity compared to the experimental values occur in the boundary layer region, with a maximum difference of 0.0062 m/s.
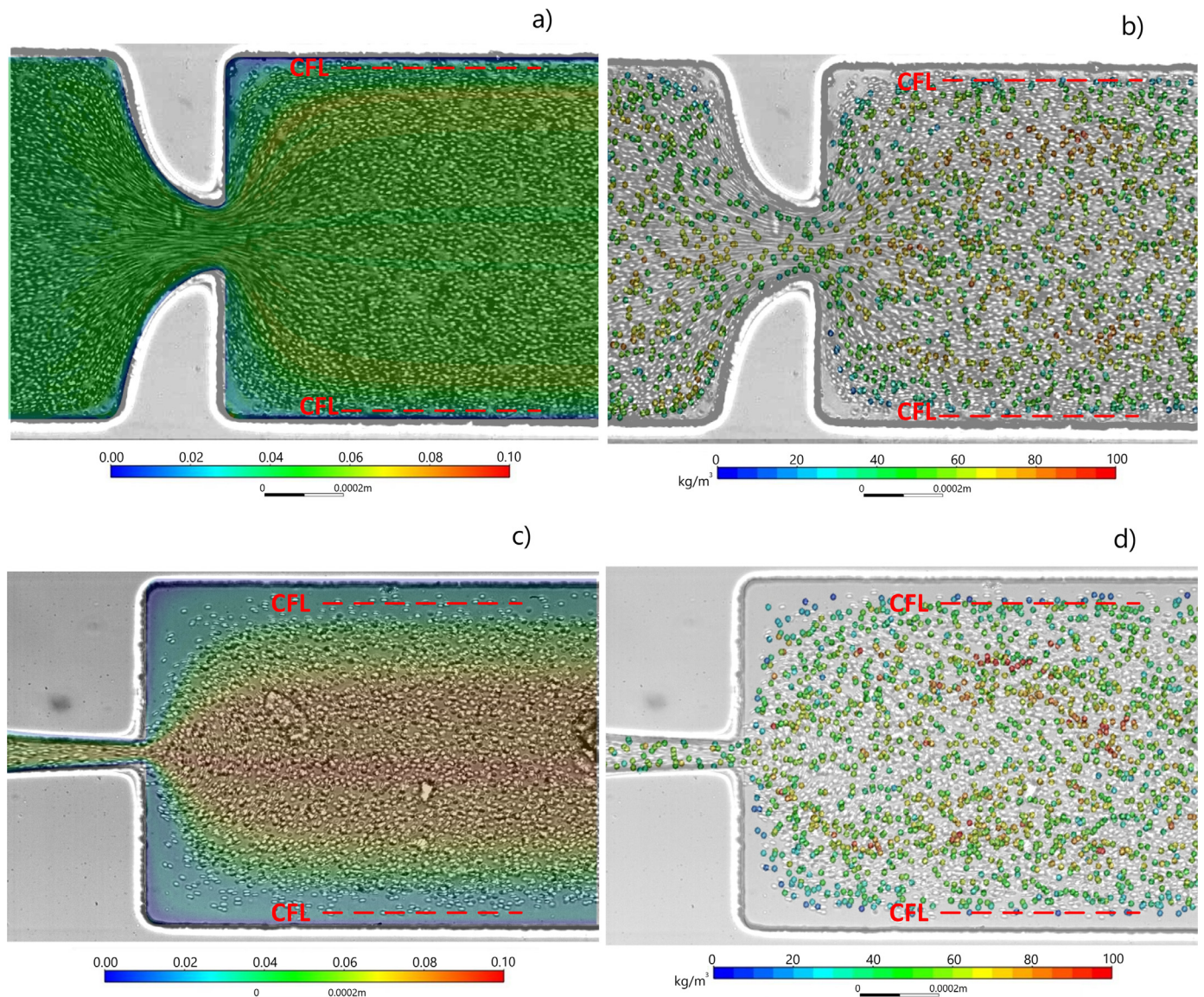
Fig. 10. Computed volume fraction distribution of RBCs in microchannel type A using a) Euler-Euler, b) Euler-Lagrange and type B c) Euler-Euler, d) Euler-Lagrange. CFD simulated RBC volume fraction (shown as colormap) compared to experimental data (shown as an image in background; note visible RBCs) in microchannel A.

The high relative error can be caused by the limitations of mesh cell size. The correct simulation of the flow behavior near the microchannel walls requires a dense mesh in that area. On the contrary, the microscale calculation requires a domain discretization of elements the size of a tenth of a micrometer, which may significantly affect the accuracy of the numerical simulation. In addition, the RBC velocity measurements in the experiment are carried out manually, and the velocity of each particle is determined by selecting each traced particle in the following video frames.

The summary of the simulation results compared to the experiment is presented in Table 3. A comparative analysis of the velocity value is presented for 15 measurement points in microchannel A and 17 points in microchannel B. For the E-E model, significant differences in the determined velocity value appear in the boundary layer area. Therefore, the calculated maximum and mean value of relative error are presented separately for all measurement points and those located only in the vessel core (marked points with a black dashed line in Fig. 5 and Fig. 6). In order to compare the numerically computed velocity values with the experimental values,

the relative error value was calculated as

$$\delta = \frac{|u^{CFD} - u^{exp}|}{u^{exp}} \tag{25}$$

where u_{CFD} represents the velocity value computed with CFD model and u_{exp} experimental velocity value calculated by manually tracking the RBC particles with the open source ImageJ software.

The E-L model enables computing the RBC velocity value in close proximity to the channel wall (10 μm distance) more precisely than does the E-E model. The relative error for velocity calculated by DPM is nearly 0% compared to above 80% for the E-E approach. As in the case of microchannel A, the high relative velocity error may result from the numerical approach used and the method of experiment analysis. As can be seen in the results presented above, the solution is not symmetrical. This occurs due to the nonsymmetrical geometry of the microchannel used in the experiment caused by the limited precision during manufacturing of the microfluidic chips. The geometry of the channel used in the simulations was adjusted to reflect the real geometry of the chip

Table 3
Microchannel validation summary.

	Microchannel A	Microchannel B
Euler-Euler model		
CFD CFL thickness (experiment)	5 μm (5 μm)	35 μm (35 μm)
Velocity mean rel. error (core flow only)	8.0%*	6.3%*
Velocity max. rel. error (core flow only)	14.3%*	11.9%*
Velocity mean rel. error	17.1%	15.8%
Velocity max. rel. error	85.3%	81.9%
Euler-Lagrange model		
CFD CFL thickness (experiment)	5 μm (5 μm)	35 μm (35 μm)
Velocity max. rel. error	5.6%	3.4%
Velocity mean rel. error	2.9%	1.9%

The values of the maximum and mean relative error for the E-E model limited to the velocity in channel core. It can be seen that in the boundary layer, at a distance of 10 μm from the wall, the maximum value of the relative error exceeds 80% for the E-E approach. The error may come from the adopted numerical simulation method, which may be influenced by the limitation of the size of numerical mesh elements and the resulting computation accuracy. At the same time, the impact on the differences between the simulation results and the experimental data may result from the method of determining the velocity of particles based on video analysis, where the particles are tracked manually.

used in the experimental phase. It can be noticed that velocity values in the channel core are slightly higher in type B microchannel despite the same inlet boundary condition, this particles behavior is caused by the influence of contraction size and also corresponds with lower velocity values near the walls.

The experimental data and numerically computed RBC distribution in microchannel type A and type B were visually compared in Section 3.4. The CFL formation caused by the Fåhræus-Lindqvist effect is visible near the wall downstream of the contraction. In the compared images, the absence of particles indicating CFL formation is visible near the microchannel wall. The calculated results of CFL thickness using E-E model and E-L model are consistent and equal approximately 5 μm for microchannel type A and 35 μm for microchannel type B. The actual RBC flow is visible, and the CFL thickness (dotted line) determined from the experimental data matches the CFD simulation. It can be noticed that there are no RBC particles near the channel wall, both in the image from the experiment and in the visualisation of CFD results. Both the E-E and E-L approaches give results consistent with the CLF thickness obtained in the experiment.

5. Conclusions

A numerical model of microchannel blood flow was built in a multiphase approach to reproduce the conditions of the in vitro experiment [16]. On the micro-scale, the Fåhræus-Lindqvist effect is particularly noticeable. To simulate this phenomenon, the multiphase Euler-Euler and Euler-Lagrange approaches have been used. The presence of contraction influences the migration of RBCs towards the channel core. Both the experiment and the numerical simulation showed that the CFL thickness downstream the contraction increased as the channel narrowing increased.

The RBC migration effect can be used, for example, to sort cells, and by knowing the relationship between the narrowing size and the CFL thickness, the bloodstream can be adjusted as needed. The conducted experiment showed that in a microchannel with a hyperbolic contraction of 54 μm, the CFL has a thickness of 5 μm downstream of the narrowing. On the other hand, when the narrowing is only 20 μm wide, the CFL increases to 35 μm.

In the analysis of the experimental data, it should be noted that the human component of analysis significantly influences the measurement results. In this case, it is the scientist who decides which

distance can be considered the end of the CFL. Comparing the CFD results with the experiment, the CFL thickness was assumed as in [16]. The obtained numerical results are in good agreement with the experimental analysis.

The μPIV-like method was used to determine the RBC velocity values to validate the model. The obtained velocity values from the hybrid Euler-Lagrange model are consistent with the flow in the microchannel. The mean relative error of velocity reaches 2.9% in microchannel A and only 1.9% in microchannel B. The Euler-Euler approach gives slightly higher values with a mean relative error value of 17.1% in channel A and 15.8% in channel B. However, the RBC velocity in the experimental analysis is determined by manually tracing a single particle in the software. This method causes inaccurate determination of the particle position between consecutive frames, leading to minor differences in determining the actual velocity value. Additionally, the error may result from the adopted numerical simulation method, which may be influenced by the limitation of the size of the numerical mesh elements and the resulting computational accuracy. The value of the mean relative error of velocity in the E-E technique is influenced by the computed value of RBC velocity in the region of the boundary layer (10 μm distance from the channel wall). In both microchannels, the relative error of velocity close to the wall is greater than 80%. In the channel core, the maximum relative error of velocity reaches 8.0% and 6.3% in channel A and B, respectively.

The predicted CFL thickness was consistent with the experimental analysis in both applied multiphase techniques. Taking into account the more accurate prediction of the velocity and concentration fields of RBC, the authors recommend using the DPM model in the E-L approach. However, attention should be paid to the discretization of the domain and check its effect on the solution obtained. In the numerical model, a commonly used simplification regarding RBC shape was assumed. The particles were modelled as rigid spheres, while, in reality, RBCs appear dumbbell-shaped in profile. In a future analysis, it will be worth considering the true shape of cells and investigating the effect of their shape on flow behavior.

Declaration of Competing Interest

The authors declare that they have no known competing financial interests or personal relationships that could have appeared to influence the work reported in this paper.

Acknowledgements

References

[1] L. Shang, Y. Cheng, Y. Zhao, Emerging droplet microfluidics, Chem. Rev. 117 (2017) 7964–8040, doi:10.1021/acs.chemrev.6b00848.

[2] G.M. Whitesides, The origins and the future of microfluidics, Nature (2006), doi:10.1016/j.agee.2012.07.026.

[3] Q. Ma, H. Ma, F. Xu, X. Wang, W. Sun, Microfluidics in cardiovascular disease research: state of the art and future outlook, Microsystems and Nanoengineering 7 (2021), doi:10.1038/s41378-021-00245-2.

[4] C.W. Shields, C.D. Reyes, P. Gabriel, P. Lpez, Microfluidic cell sorting: a review of the advances in the separation of cells from debulking to rare cell isolation, Lab Chip 2015 (2015), doi:10.1039/c4lc01246a.

[5] F. Khodaee, S. Movahed, N. Fatouraee, F. Daneshmand, Numerical simulation of separation of circulating tumor cells from blood stream in deterministic lateral displacement (dld) microfluidic channel, Journal of Mechanics 32 (2018), doi:10.1017/jmech.2015.91.

[6] X. Li, W. Chen, G. Liu, W. Lu, J. Fu, Continuous-flow microfluidic blood cell sorting for unprocessed whole blood using surface-micromachined microfiltration membranes, Lab Chip 14 (2014) 2565–2575, doi:10.1039/c4lc00350k.

[7] E. Kucukal, Y. Man, U.A. Gurkan, B.E. Schmidt, Blood flow velocimetry in a microchannel during coagulation using particle image velocimetry and wavelet-based optical flow velocimetry, J Biomech Eng 143 (2021), doi:10.1115/1.4050647.

[8] S.Z. Hoque, D.V. Anand, B.S.V. Patnaik, A dissipative particle dynamics simulation of a pair of red blood cells in flow through a symmetric and an asymmetric bifurcated microchannel, Computational Particle Mechanics (2022), doi:10.1007/s40571-021-00453-7.

[9] Y.S. Zhang, A. Arneri, S. Bersini, S.R. Shin, K. Zhu, Z. Goli-Malekabadi, J. Aleman, C. Colosi, F. Busignani, V. Dell'Erba, C. Bishop, T. Shupe, D. Demarchi, M. Moretti, M. Rasponi, M.R. Dokmeci, A. Atala, A. Khademhosseini, Bioprinting 3d microfibrous scaffolds for engineering endothelialized myocardium and heart-on-a-chip, Biomaterials 110 (2016) 45–59, doi:10.1016/j.biomaterials.2016.09.003.

[10] M.P. Wolf, G.B. Salieb-Beugelaar, P. Hunziker, Pdms with designer functionalities properties, modifications strategies, and applications, Prog Polym Sci 83 (2018) 97–134, doi:10.1016/j.progpolymsci.2018.06.001.

[11] J. Kim, J.F. Antaki, M. Massoudi, Computational study of blood flow in microchannels, J Comput Appl Math 292 (2016) 174–187, doi:10.1016/j.cam.2015.06.017.

[12] G.J. Arthurs, M. Sudhakar, Carbon dioxide transport, Continuing Education in Anaesthesia, Critical Care and Pain 5 (2005) 207–210, doi:10.1093/bjaceaccp/mki050.

[13] P.D. Morris, D. Ryan, A.C. Morton, R. Lycett, P.V. Lawford, D.R. Hose, J.P. Gunn, Virtual fractional flow reserve from coronary angiography: modeling the significance of coronary lesions: results from the virtu-1 (virtual fractional flow reserve from coronary angiography) study, JACC: Cardiovascular Interventions 6 (2013) 149–157, doi:10.1016/j.jcin.2012.08.024.

[14] R. Fåhræus, T. Lindqvist, The viscosity of the blood in narrow capillary tubes, Am. J. Physiol. 96 (1931) 562–568.

[15] T. Yaginuma, M.S.N. Oliveira, R. Lima, T. Ishikawa, T. Yamaguchi, Human red blood cell behavior under homogeneous extensional flow in a hyperbolic-shaped microchannel, Biomicrofluidics 7 (2013) 054110, doi:10.1063/1.4820414.

[16] R.O. Rodrigues, R. Lopes, D. Pinho, A.I. Pereira, V. Garcia, S. Gassmann, P.C. Sousa, R. Lima, In vitro blood flow and cell-free layer in hyperbolic microchannels: visualizations and measurements, Biochip J 10 (2016) 9–15, doi:10.1007/s13206-016-0102-2.

[17] J. Huang, R.W. Lyczkowski, D. Gidaspow, Pulsatile flow in a coronary artery using multiphase kinetic theory, J Biomech (2009) doi:10.1016/j.jbiomech.2009.01.038.

[18] B. Melka, W.P. Adamczyk, M. Rojczyk, M.L. Nowak, M. Gracka, A.J. Nowak, A. Golda, R.A. Bialecki, Z. Ostrowski, Numerical investigation of multiphase blood flow coupled with lumped parameter model of outflow, Int. J. Numer. Methods Heat Fluid Flow 30 (2019) 228–244, doi:10.1108/HFF-04-2019-0279.

[19] H. Aryan, B. Beigzadeh, M. Siavashi, Euler-lagrange numerical simulation of improved magnetic drug delivery in a three-dimensional ct-based carotid artery bifurcation, Comput Methods Programs Biomed 219 (2022) 106778, doi:10.1016/j.cmpb.2022.106778.

[20] W.-T. Wu, F. Yang, J.F. Antaki, N. Aubry, M. Massoudi, Study of blood flow in several benchmark micro-channels using a two-fluid approach, Int J Eng Sci 95 (2015) 49–59, doi:10.1016/j.ijengsci.2015.06.004.

[21] T. Franke, R.H.W. Hoppe, C. Linsenmann, L. Schmid, C. Willbold, A. Wixforth, F.L. Schmid, A. Wixforth, R.H.W. Hoppe, C. Linsenmann, C. Willbold, Numerical simulation of the motion of red blood cells and vesicles in microfluidic flows, Comput Visual Sci 14 (2011) 167–180, doi:10.1007/s00791-012-0172-1.

[22] T. Wu, Q. Guo, H. Ma, J.J. Feng, The critical pressure for driving a red blood cell through a contracting microfluidic channel, Theor. Appl. Mech. Lett. 5 (2015) 227–230, doi:10.1016/j.taml.2015.11.006.

[23] J. Mauer, S. Mendez, L. Lanotte, F. Nicoud, M. Abkarian, Flow-induced transitions of red blood cell shapes under shear, Physical Review Letters, American Physical Society, 121 (11) (2018).

[24] P. Giri, K. Chandran, K. Muralidhar, I.S. Dalal, Effects of coupling of mass transport and blood viscosity models for microchannel flows, J Nonnewton Fluid Mech 302 (2022), doi:10.1016/j.jnnfm.2022.104754.

[25] J. Jung, A. Hassanein, Three-phase CFD analytical modeling of blood flow, Medical Engineering & Physics 30 (2008) 91–103, doi:10.1016/j.medengphy.2006.12.004.

[26] C. Wen, Y. Yu, Mechanics of fluidization, The Chemical Engineering Progress Symposium Series 67 (1966) 100–111.

[27] J. Jung, A. Hassanein, R.W. Lyczkowski, Hemodynamic computation using multiphase flow dynamics in a right coronary artery, Ann Biomed Eng (2006), doi:10.1007/s10439-005-9017-0.

[28] W.P. Adamczyk, A. Klimanek, R.A. Bialecki, G. Wecel, P. Kozolub, T. Czakiert, Comparison of the standard euler-euler and hybrid euler-lagrange approaches for modeling particle transport in a pilot-scale circulating fluidized bed, Particuology 15 (2014) 129–137, doi:10.1016/j.partic.2013.06.008.

[29] Ansys academic research„ Release 17.2, Help System, ANSYS Fluent Theory Guide, ANSYS, Inc. (2020).

[30] F.K. Benra, H.J. Dohmen, J. Pei, S. Schuster, B. Wan, A comparison of one-way and two-way coupling methods for numerical analysis of fluid-structure interactions, J Appl Math 2011 (2011), doi:10.1155/2011/853560.

[31] N.M. Zahari, M.H. Zawawi, L.M. Sidek, D. Mohamad, Z. Itam, M.Z. Ramli, A. Syamsir, A. Abas, M. Rashid, Introduction of discrete phase model (DPM) in fluid flow: a review, AIP Conf Proc 2030 (2018), doi:10.1063/1.5066875.

[32] D. Gidaspow, Multiphase flow and fluidization, J Nonnewton Fluid Mech 55 (1994) 498, doi:10.1016/0377-0257(94)80007-3.

[33] S.A. Morsi, A.J. Alexander, An investigation of particle trajectories in two-phase flow systems, J Fluid Mech 55 (1972) 193–208, doi:10.1017/S0022112072001806.

[34] D. Pinho, L. Campo-Deaño, R. Lima, F.T. Pinho, In vitro particulate analogue fluids for experimental studies of rheological and hemorheological behavior of glucose-rich rbc suspensions, Biomicrofluidics 11 (2017), doi:10.1063/1.4998190.

[35] A. Passos, J.M. Sherwood, E. Kaliviotis, R. Agrawal, C. Pavesio, S. Balabani, The effect of deformability on the microscale flow behavior of red blood cell suspensions, Physics of Fluids 31 (2019), doi:10.1063/1.5111189.

[36] M. Depond, B. Henry, P. Buffet, P.A. Ndour, Methods to investigate the deformability of rbc during malaria, Front Physiol 10 (2020), doi:10.3389/fphys.2019.01613.

[37] F. Yaya, J. Römer, A. Guckenberger, T. John, S. Gekle, T. Podgorski, C. Wagner, Vortical flow structures induced by red blood cells in capillaries, Microcirculation 28 (2021), doi:10.1111/micc.12693.

[38] S. Ebrahimi, P. Bagchi, A computational study of red blood cell deformability effect on hemodynamic alteration in capillary vessel networks, Sci Rep 12 (2022), doi:10.1038/s41598-022-08357-z.

[39] T. Kruger, D. Holmes, P.V. Coveney, Deformability-based red blood cell separation in deterministic lateral displacement devices-a simulation study, Biomicrofluidics 8 (2014), doi:10.1063/1.4897913.

[40] A. Bohiniková, I. Jančigová, I. Cimrák, Modeling red blood cell viscosity contrast using inner soft particle suspension, Micromachines (Basel) 12 (2021), doi:10.3390/mi12080974.

[41] Y. Wang, J. Zhan, W. Bian, X. Tang, M. Zeng, Local hemodynamic analysis after coronary stent implantation based on euler-lagrange method, J Biol Phys 47 (2021) 143–170, doi:10.1007/s10867-021-09571-y.

[42] K. Tatsumi, S. Noguchi, A. Tatsumi, R. Kuriyama, K. Nakabe, Particle and rigidized red blood cell concentration distributions in microchannel flows, Physics of Fluids 31 (2019), doi:10.1063/1.5111201.

[43] K. Chandran, I.S. Dalal, K. Tatsumi, K. Muralidhar, Numerical simulation of blood flow modeled as a fluid- particulate mixture, J Nonnewton Fluid Mech 285 (2020), doi:10.1016/j.jnnfm.2020.104383.

[44] R. Lima, C.S. Fernandes, R. Dias, T. Ishikawa, Y. Imai, T. Yamaguchi, Microscale flow dynamics of red blood cells in microchannels: an experimental and numerical analysis, Computational Methods in Applied Sciences 19 (2011) 297–309, doi:10.1007/978-94-007-0011-6_17.

[45] W.S. Rasband, ImageJ, U. S. National Institutes of Health, Bethesda, Maryland, USA„ 1997, Source:. [Accessed 20 April 2022] https://imagej.nih.gov/ij/.